ISIJ International, Vol. 66 (2026), No. 8, pp. 915–924
https://doi.org/10.2355/isijinternational.ISIJINT-2026-038

Systematic Study of Rapid Solidification in Laser Powder-bed Fusion of Stainless Steels to Verify Applicability of Columnar-equiaxed Transition

Kishin FUKUSHIMA,[1)] Masayuki OKUGAWA,[1,2)*] Yuichiro MIYATA,[1)] Rei MIYAWAKI,[1)] Yuheng LIU,[1)] Yuichiro KOIZUMI[1,2)] and Takayoshi NAKANO[1,2)]

1) Graduate School of Engineering, The University of Osaka, 2-1 Yamadaoka, Suita, Osaka, 565-0871 Japan.
2) 3DPTec Integrated Center, The University of Osaka, 2-1 Yamadaoka, Suita, 565-0871 Japan.

(*Received February 17, 2026; Accepted June 2, 2026; Advance online published June 10, 2026; Published July 15, 2026*)

In recent years, microstructural control in powder-bed fusion (PBF)-type metal additive manufacturing (AM) has attracted considerable attention. The solidification microstructure is generally described by the columnar-equiaxed transition (CET) criterion. However, we previously reported that austenitic stainless steels (SSs) melted by beam irradiation for PBF exhibit an opposite trend to the CET criteria. It is essential to systematically understand the microstructural formation behavior under the rapid cooling and high-velocity flow conditions unique to the PBF process to obtain guidelines for microstructural control of SSs. In this study, we systematically investigated the solidification behavior in laser-melted regions of austenitic, ferritic, and martensitic SSs to elucidate the dominant factors governing microstructural formation. The liquidus–solidus temperature difference (ΔT_0), which varies among the SSs, was examined as a key parameter characterizing the alloy-dependent solidification behavior. Based on the digital twin analysis, we proposed that the CET criteria serve as a guideline for ferritic and martensitic SSs in the PBF process, whereas they cannot be used for austenitic SSs, which exhibit the opposite trend to the CET criteria. Additionally, the machine-learning analysis, *i.e.*, random forest, indicated that concentrations of Si, Mn, and C particularly affect microstructural formation.

KEY WORDS: additive manufacturing; laser powder-bed fusion; stainless steel; computational thermal-fluid dynamics; random forest.

1. Introduction

In recent years, Additive Manufacturing (AM) technology has garnered significant attention because it enables the fabrication of products with complex internal geometries and can reduce material consumption.[1,2)] Among the various metal AM techniques, powder-bed fusion (PBF) is commonly used.[3–13)] In the PBF process, a part is fabricated by repeating powder spreading and selectively melting and solidifying by laser- or electron-beams along two-dimensional slice data derived from 3D CAD data. The PBF type AM technique has been applied to stainless steels (SSs) for a wide range of applications, such as aerospace, power plants, and medical implants.[14–20)]

In the PBF process, the crystal orientation can be controlled by the heat source scanning strategy,[21–25)] and many researchers have investigated the relationship between PBF process parameters and microstructures in SSs in recent years.[16,18,19)] This allows us to control the crystal microstructure at each point of a component by adjusting the beam conditions. Controlling both part shape and crystal orientation allows us to create new materials and improve performance compared to conventional processes.

The microstructure obtained in the PBF process for metals is a solidification microstructure. Solidification microstructure is generally considered to be determined by the combination of the temperature gradient (G) at the solid/liquid interface and the solidification rate (R) according to the Columnar-Equiaxed Transition (CET) criteria.[26–29)] The transition criterion is expressed by Eq. (1):

$$\frac{G^n}{R} = a\left(8.6\Delta T_0 \frac{N_0^{1/3}}{n+1}\right)^n \quad \text{..... (1)}$$

Here, n and a are alloy constants, ΔT_0 is the temperature difference between the liquidus and solidus lines at equi-

* Corresponding author: E-mail: okugawa@mat.eng.osaka-u.ac.jp

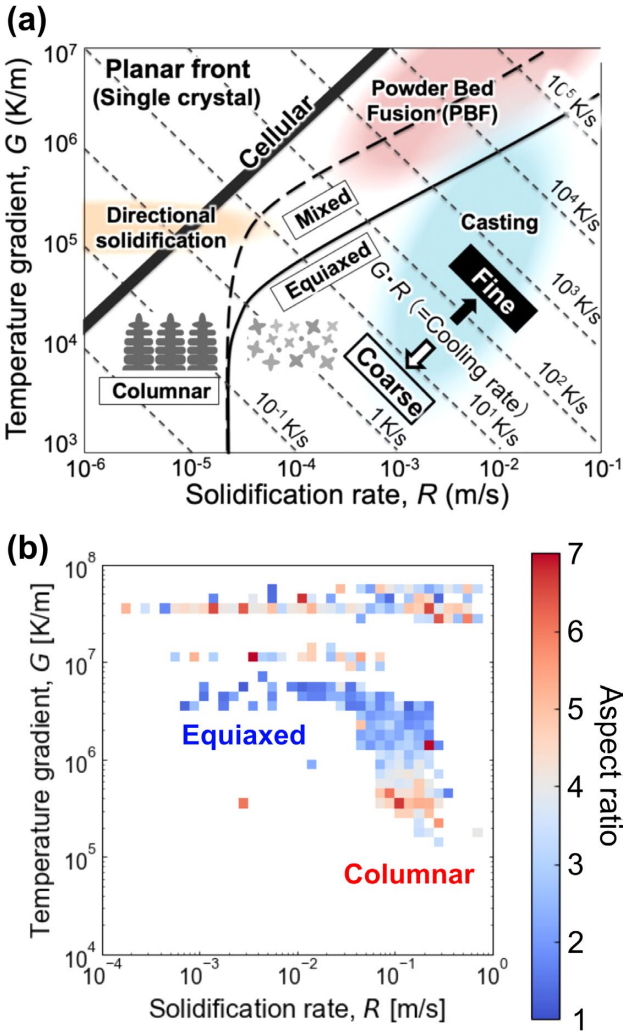

Fig. 1. (a) Typical solidification maps for microstructure control based on Hunt's columnar-equiaxed transition (CET).[10,26] Reproduced from Koizumi *et al.*,[10] under the CC BY 4.0 license. (b) Solidification map of electron-beam melted 316L SS colored by average aspect ratio calculated for each mesh of the double logarithmic grid using the points of solidification condition within each mesh.[33] Reproduced from Miyata *et al.*,[33] under the CC BY 4.0 license. (Online version in color.)

librium, and N_0 represents the heterogeneous nucleation frequency from the liquid phase. Columnar crystals form when the left-hand side of Eq. (1) is larger, while equiaxed crystals form when the right-hand side is larger. **Figure 1**(a) schematically illustrates the conventional interpretation of the *G*–*R* map: columnar crystals are expected in the high-*G* and low-*R* region, whereas equiaxed grains are expected in the low-*G* and high-*R* region, with the CET boundary determined by the alloy-dependent parameters in Eq. (1). Whether such a CET criterion is applicable is particularly important in AM processes, as solidification occurs under unique conditions.[30–33]

However, we previously investigated the relationship between solidification microstructure and solidification conditions of the austenitic SSs, *i.e.*, 304 and 316L,[33] and found that the inverse CET microstructural formation occurs in the PBF process: equiaxed grains were observed more frequently in the high-*G* and low-*R* region rather than in the low-*G* and high-*R* region, contrary to the conventional CET criterion (Fig. 1(b)). The CtFD simulation suggests that the high fluid velocity unique to the PBF process promotes dendrite fragmentation and transport of the fragments, which can apparently reverse the trend of equiaxed grain formation.[33] It is important to systematically understand the microstructural formation behavior under rapid solidification conditions to obtain guidelines for microstructural control in the PBF of SSs.

In this study, we systematically investigated the solidification behavior in laser-melted regions of austenitic, ferritic, and martensitic SSs to elucidate the dominant factors governing microstructural formation using a combined experimental and computational approach. The liquidus–solidus temperature difference (ΔT_0), which varies among the SSs, was examined as a key parameter characterizing the alloy-dependent solidification behavior. In addition, we conducted a machine-learning analysis to provide an alloy design guideline that considers microstructure control in the PBF process.

Table 1. Alloy Compositions of stainless steels used in this study (mass%).

	Grade	C	Cr	Mn	Mo	Ni	Si	P	S	Co	Cu	N	Ti	Nb	Fe
Austenitic	304	0.036	18.03	1.29	0	7.82	0.37	0.041	0.02	0.21	–	–	–	–	Bal.
	304L	0.019	19.38	1.85	0	9.22	0.26	0.038	0.017	0.2	–	–	–	–	
	316	0.04	16.96	1.33	2.06	10.07	0.21	0.034	0.028	0.2	–	–	–	–	
	316L	0.015	16.92	1.53	2.03	11.95	0.47	0.031	0.003	0.25	–	–	–	–	
	321	0.02	17.13	2.00	0	9.02	0.37	0.034	0.027	–	–	–	0.10	–	
Ferritic	430	0.09	16.09	0.81	0	0.23	0.26	0.03	0.003	–	–	–	–	–	
	443J1	0.012	20.75	0.08	–	–	0.09	0.026	0.002	–	0.43	0.012	0.34	–	
	444	0.004	18.84	0.14	1.79	0.1	0.14	0.03	0	–	–	0.011	0.14	0.19	
Martensitic	403	0.12	11.67	0.41	0	0.29	0.28	0.028	0.019	–	0	–	–	–	
	410	0.06	12.47	0.22	0	0.06	0.41	0.021	0.002	–	–	–	–	–	
	420J2	0.35	12.16	0.41	–	–	0.46	0.028	0.018	–	–	–	–	–	
	440C	0.98	16.06	0.33	0.17	0.26	0.29	0.032	0.001	–	–	–	–	–	

2. Method

First, we investigated microstructural formations of the SSs melted by laser beam irradiation. **Tables 1** and **2** show the alloy compositions of the SSs and the solidus and liquidus temperatures and ΔT_0 calculated using an alloy physical property calculation software (Sente software JMatPro v11.2), respectively. The single-bead formation experiments have been conducted using the PBF machine (EOS, M290). The beam power P and scanning speed V were 360 W and 600 mm s^{-1}, respectively. The cross-sections of the formed melt pools were observed using a field emission scanning electron microscope (FE-SEM, JEOL, JSM6500), and crystal orientation analysis was performed using electron backscatter diffraction (EBSD).

Table 2. Liquidus temperature T_L, Solidus temperature T_S, and their differences ΔT_0 of each steel.

	Grade	Liquidus temperature T_L (K)	Solidus temperature T_S (K)	ΔT_0 (K)
Austenitic	304	1 738.73	1 629.85	108.88
	304L	1 730.58	1 619.85	110.73
	316	1 726.50	1 604.85	121.65
	316L	1 719.36	1 659.85	59.51
	321	1 730.24	1 629.85	100.39
Ferritic	430	1 773.44	1 684.85	88.59
	443J1	1 773.10	1 549.85	223.25
	444	1 779.81	1 589.85	189.96
Martensitic	403	1 775.59	1 499.85	275.74
	410	1 781.84	1 679.85	101.99
	420J2	1 752.36	1 579.85	172.51
	440C	1 691.33	1 554.85	136.48

The computational thermal fluid dynamics (CtFD) simulations were performed to evaluate solidification conditions using a commercial 3D thermo-fluid analysis software (Flow Science FLOW-3D with Flow-3D Weld module). **Table 3** shows the parameters used for the simulations. Most of the parameters of physical properties were evaluated by calculation using an alloy physical property calculation software (Sente software JMatPro v11.2). For the heat transfer coefficient, the value for 304L SS[34] was used for all SSs, and for the heat of vaporization and vaporization temperature, the values for pure Fe[35] were used. Beam power P and scanning speed V were identical to the experiments: P = 360 W and V = 600 mm s^{-1}. To reduce computation time, a 10 × 10 × 10 μm mesh was applied near the laser-irradiated region, while a 40 × 40 × 40 μm mesh was used elsewhere. The fine mesh size is consistent with that used in our previous CtFD studies on PBF-LB[30,31] and is sufficiently small relative to the melt pool dimensions (approximately 100–200 μm in depth and 200–300 μm in width) to resolve the temperature field at the solid/liquid interface. The substrate temperature was initially set to 300 K. The continuity boundary condition was applied to all boundaries except the top surface, and the top surface was maintained at a constant pressure of 1.013×10^5 Pa. The Fresnel coefficient ε, which determines beam absorption efficiency, was used as a fitting parameter to reproduce the experimentally observed melt pool shapes. Solidification conditions were evaluated from the time evolution of the temperature field.

The multiple regression analysis using a random forest was performed to obtain guidelines for alloy design. The Random Forest Regressor within the Python library scikit-learn was used for the analysis. The concentrations of C, Cr, Mn, Mo, Ni, and Si were used as variables, and the correlations with the average aspect ratio and the average grain size were examined to investigate the contribution of alloy composition to microstructure formation. The average aspect ratio and grain size were calculated by normalizing

Table 3. Parameters used in CtFD simulations.

	Grade	Thermal conductivity (300 K)	Specific heat (300 K)	Surface tension (T_s)	Viscosity (T_s)	Compressibility (T_L)	Density (300 K)	Heat transfer	Latent heat of vaporization	Saturation temperature (1 atm)
		(W m^{-1} K^{-1})	(J kg^{-1} K^{-1})	(kg s^{-2})	(g m^{-1} s^{-1})	(Pa^{-1})	(kg m^{-3})	(W m^{-2} K^{-1})	(J kg^{-1})	(K)
Austenitic	304	15.47	451.3	1.798	7.858	9.32×10^{-12}	7 997	210	6.34×10^6	3 273
	304L	15.06	450.1	1.779	8.074	9.25×10^{-12}	7 960	210	6.34×10^6	3 273
	316	14.33	446.1	1.802	8.208	9.16×10^{-12}	8 021	210	6.34×10^6	3 273
	316L	13.90	446.1	1.798	8.457	9.11×10^{-12}	8 002	210	6.34×10^6	3 273
	321	14.93	451.2	1.750	7.965	9.30×10^{-12}	7 958	210	6.34×10^6	3 273
Ferritic	430	17.50	450.8	1.798	7.193	9.65×10^{-12}	7 725	210	6.34×10^6	3 273
	443J1	17.88	451.6	1.590	10.35	9.59×10^{-12}	7 696	210	6.34×10^6	3 273
	444	17.96	447.7	1.815	10.88	9.54×10^{-12}	7 743	210	6.34×10^6	3 273
Martensitic	403	17.48	451.3	1.857	8.983	9.71×10^{-12}	7 743	210	6.34×10^6	3 273
	410	17.49	451.4	1.849	7.800	9.70×10^{-12}	7 739	210	6.34×10^6	3 273
	420J2	17.42	476.2	1.803	6.542	9.74×10^{-12}	7 717	210	6.34×10^6	3 273
	440C	17.63	993.2	1.863	6.881	9.74×10^{-12}	7 822	210	6.34×10^6	3 273

the grain data derived from EBSD analysis.

3. Results and Discussion

Figures 2(a1) and 2(a2) show the track surface image and corresponding height image of the laser irradiated 316L SS as a typical example. The start points of the beam irradiated in all samples formed a shape protruding above the non-irradiated regions, while the end points formed a shape recessed below the non-irradiated regions. This inhomogeneity is supposed to be caused by flow within the melt pool owing to the Marangoni force:[36] the region directly irradiated by a laser beam is at the highest temperature, while the region after the beam has passed is relatively cooler. Generally, the surface tension of molten metal decreases with increasing temperature, and the surface tension is lower in the beam-irradiation region and higher in the region after the beam has passed. Consequently, a molten metal flow occurs because of the surface tension differences. At the start point of beam irradiation, there is only inflow from the front, resulting in a raised shape. Conversely, at the end point of beam irradiation, there is only outflow toward the rear, resulting in a depressed shape.

The cross-sectional microstructures of the central regions of laser-scanned SSs perpendicular to the beam-scanning direction were investigated using SEM–EBSD. Figures 2(b)–2(m) show the cross-sectional inverse pole figure (IPF) *z* orientation maps of the melt region. The various microstructures are formed depending on the type of steel: epitaxial growth from the non-melted region was observed in most SSs. The mixed microstructures of columnar crystals and equiaxed grains are formed in 321 and 403 SSs (Figs. 2(f) and 2(i)). On the other hand, the equiaxed microstructure formed via martensitic transformation with diameters of approximately 3 μm appeared in the melt regions in 420J2 SS (Fig. 2(l)).

Figures 3(a1)–3(a3) show snapshots of the CtFD simulation of 316L SS colored by temperature and solid fraction. P and V were 360 W and 600 mm s^{-1}, respectively. An elongated teardrop-shaped melt pool was formed, and a keyhole-type deeply melting behavior can be seen. The Fresnel coefficient ε was used as a fitting parameter to reproduce the morphology of the experimentally observed melt region. Figures 3(b)–3(m) compare the melt regions of the SSs. Setting the Fresnel coefficient ε = 0.075–0.150 successfully reproduced the experimental melt pool shape, and the coefficients are similar to those reported in previous studies.[30,31]

The temperature gradient (G) and solidification rate (R) were evaluated from temporal changes in the temperature distribution during the experimentally validated CtFD simulations. **Figure 4**(a) shows the cross-sectional melt pools colored according to G and R of the 316L SS as a typical example. To output the temperature conditions at the solid/liquid interface in the melt pool, only the data of the mesh with a solid phase ratio of ~0.5 in the CtFD simulation were plotted. In the regions near the melt pool boundary, the G was the highest, which decreased as the liquid/solid interface shifted toward the center of the melt pool. Solidification near the melt pool boundary occurs as the unmelted bulk outside facilitates heat removal. Conversely, solidification inside of the melt region occurs

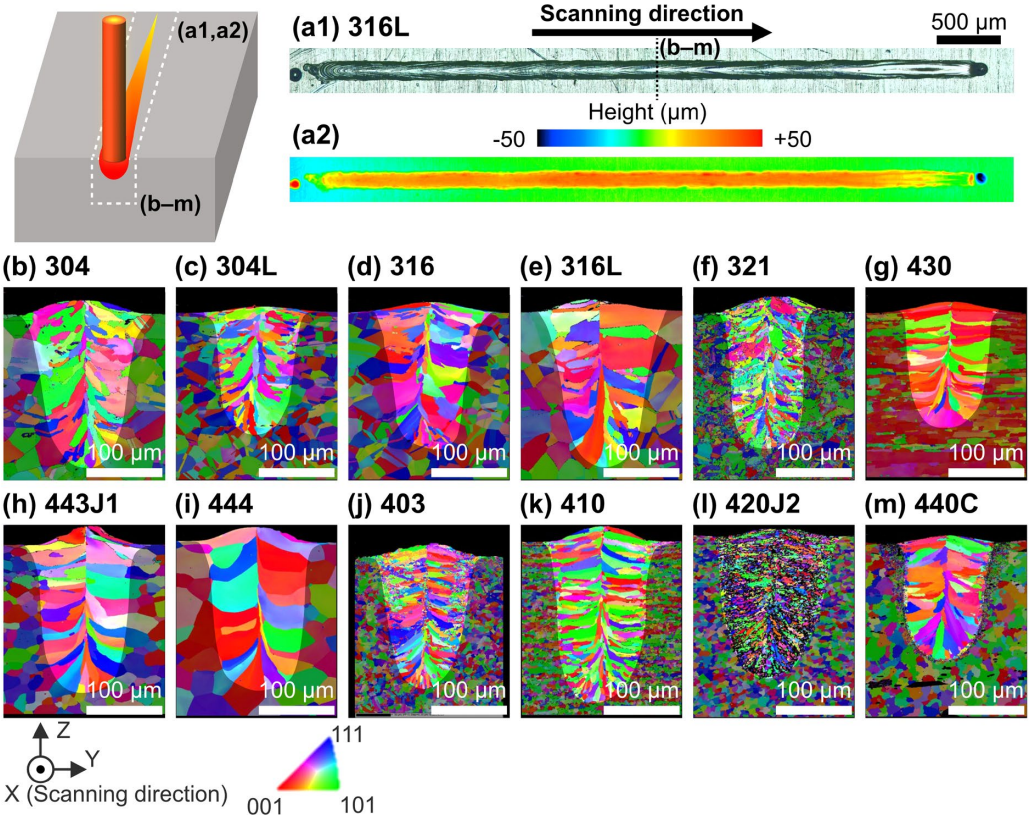

Fig. 2. (a1) Surface image of laser-beam irradiated region in 316L SS and (a2) corresponding height map. (b–m) Cross-sectional SEM-EBSD inverse pole figure (IPF) z-orientation maps of the central regions of laser-scanned SSs perpendicular to the beam-scanning direction. (Online version in color.)

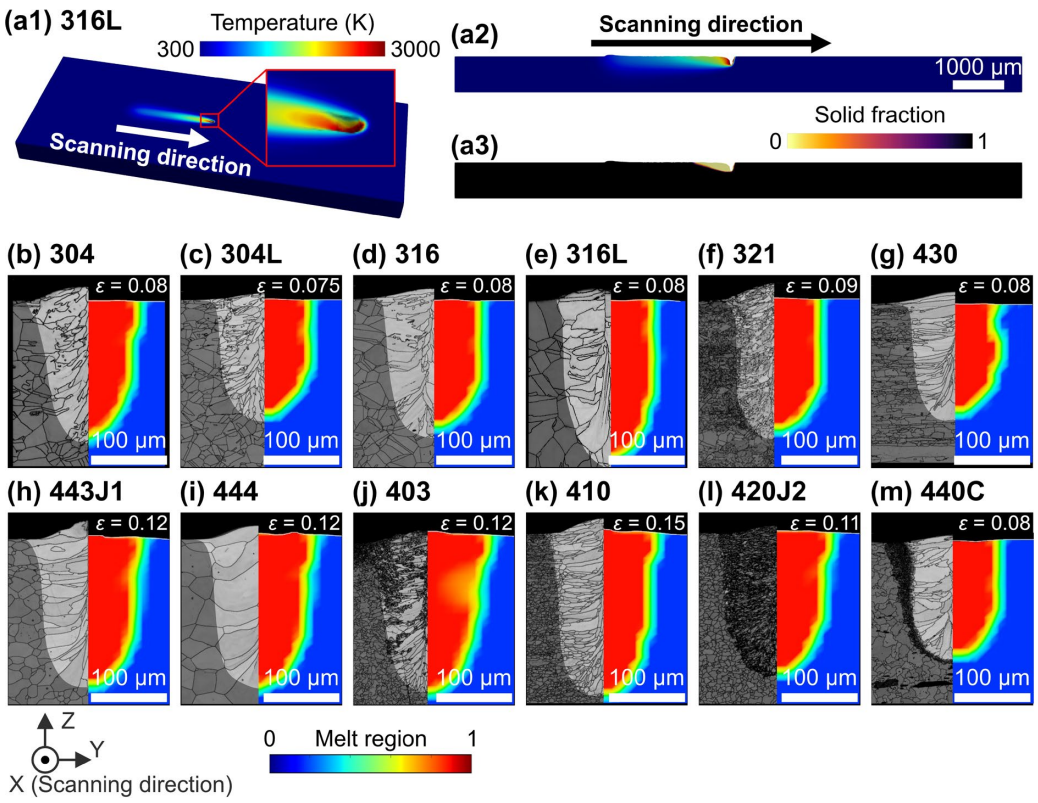

Fig. 3. (a1–a3) Snapshots of CtFD laser irradiation simulation for 316L SS colored by temperature and solid fraction. (b–m) Comparison of experimentally observed and simulated melt pools of SSs formed by laser beam scanning. The beam power P and scanning speed V were 360 W and 600 mm s^{-1}, respectively. (Online version in color.)

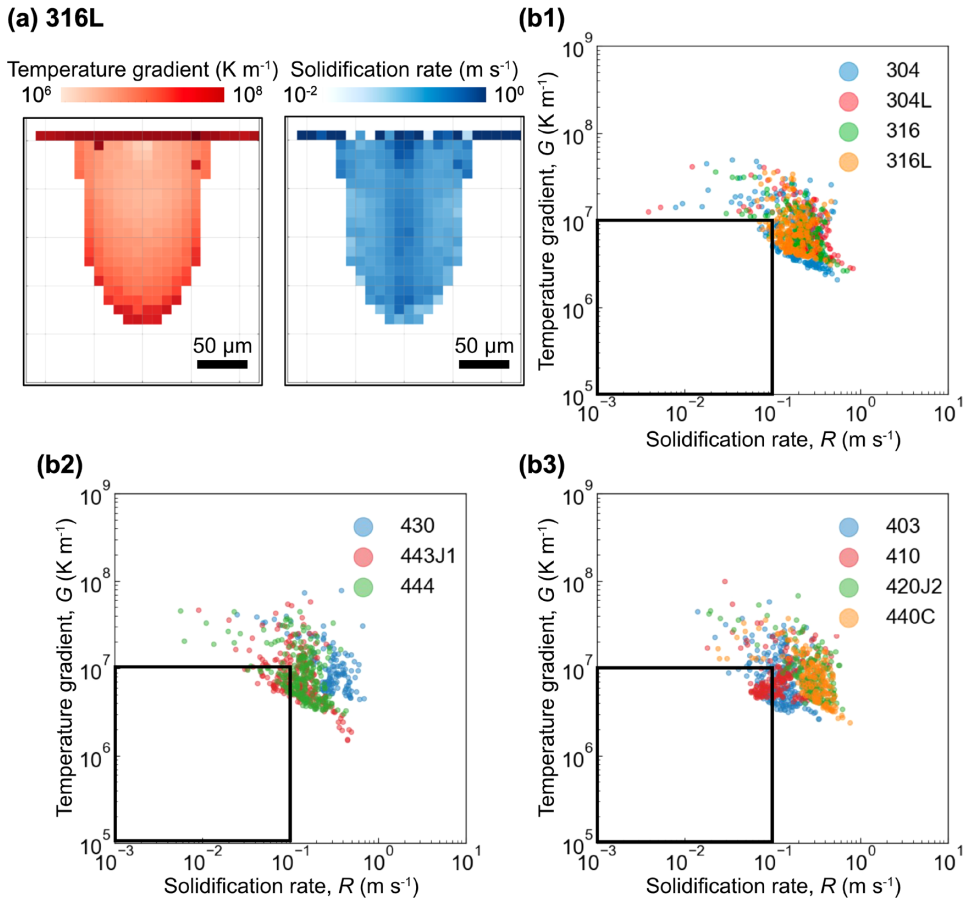

Fig. 4. (a) CtFD simulated cross-sectional melt region of 316L SS colored by a temperature gradient G and a solidification rate R. G–R plots of (b1) austenitic, (b2) ferritic, and (b3) martensitic SSs. (Online version in color.)

surrounded by metal solid just above its melting point, making heat removal difficult and leading to a smaller temperature gradient. On the other hand, the R was the lowest near the melt pool boundary and increased as the interface approached the center of the melt region. The tendency of the distribution of the solidification conditions is consistent across all of the SSs investigated in the present study. It is noteworthy that the G became extremely large at the surface of the melt pool, suggesting that the surface region was cooled mainly by external thermal radiation rather than thermal diffusion through the metal substrate. During the stacking of the upper layer in the PBF process, remelting and resolidification occur in the surface regions. The surface regions are not critical for controlling the solidification microstructure; consequently, the top 10 μm was excluded from subsequent analyses.

Figures 4(b1)–4(b3) show the plots in the G–R space of the solidification conditions of austenitic (Fig. 4(b1)), ferritic (Fig. 4(b2)), and martensitic SSs (Fig. 4(b3)). Except for the surface regions, most of the regions solidified under G and R in the ranges of 10^6–10^8 K m^{-1} and 10^{-2}–10^0 m s^{-1}, respectively. Almost all of the conditions are out of the range of black squares in Figs. 4(b1)–4(b3), which indicates the solidification conditions assumed for the conventional solidification map.[26)]

Figures 5 and **6** show the G–R plot of SSs colored according to the aspect ratio of the formed local microstructure and flow velocity when a liquid/solid interface passes through the local regions, respectively. Many of the plot points overlap if plotted as is because of a large amount of data. Thus, the areas of the G–R plots were divided into 50 × 50 regions in a double logarithmic scale, and the aver-

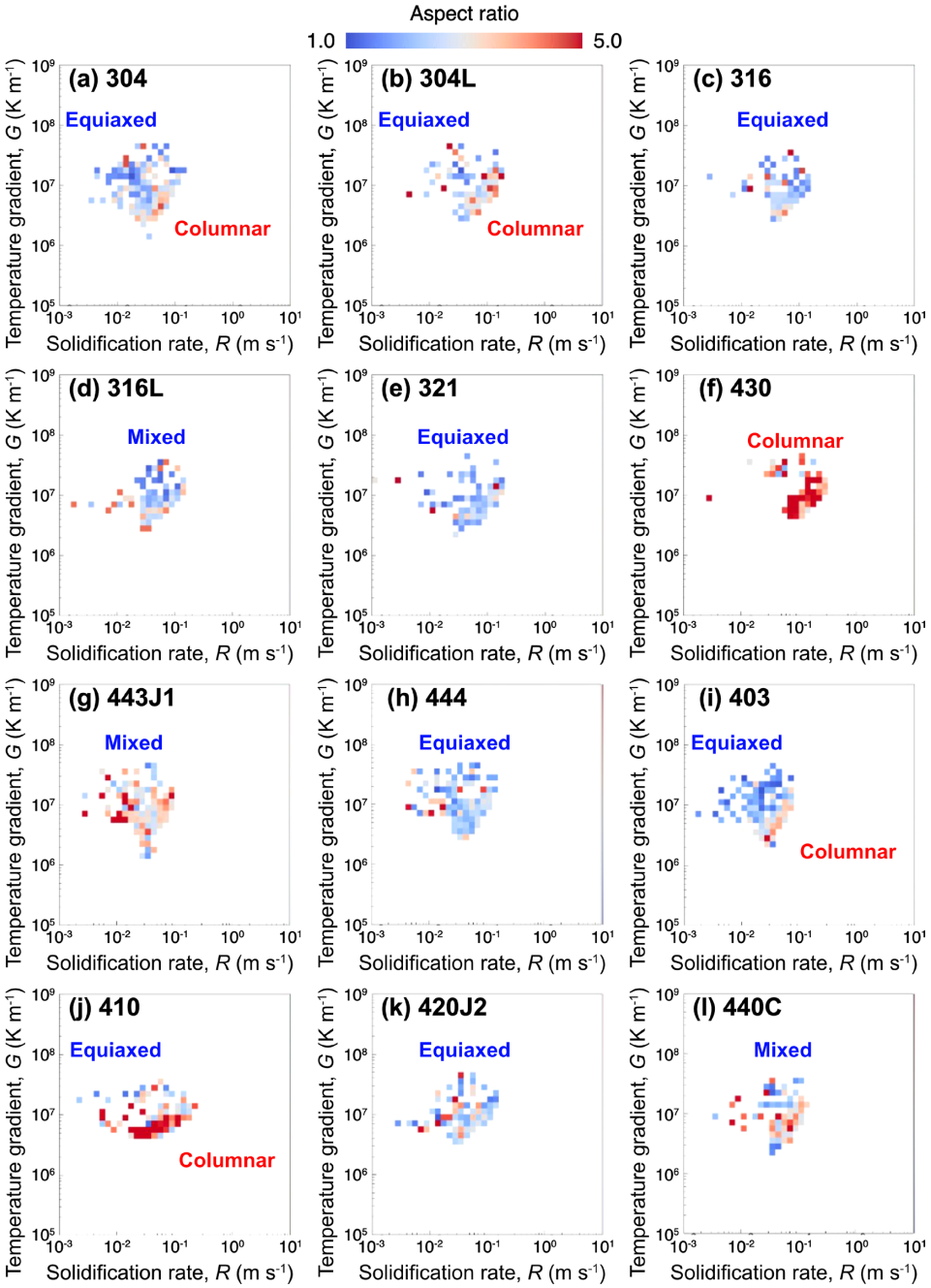

Fig. 5. Average aspect ratios of SSs calculated for each mesh of the double-logarithmic grid using the points of solidification condition within each mesh. (Online version in color.)

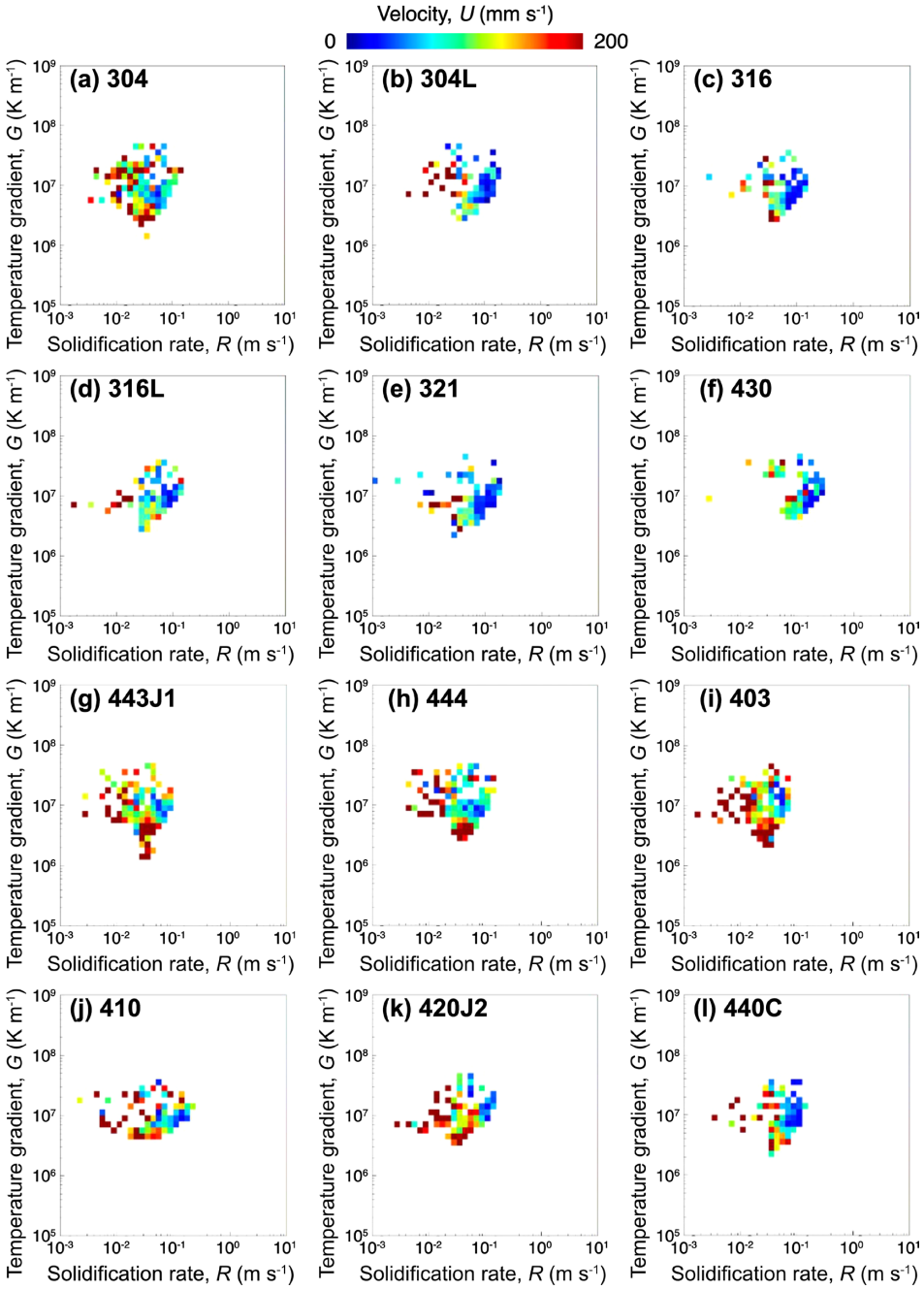

Fig. 6. Average fluid velocities of SSs calculated for each mesh of the double-logarithmic grid using the points of solidification condition within each mesh. (Online version in color.)

age aspect ratio and flow velocity within each divided region were plotted. According to the CET criteria,[26–29] columnar crystals form under high G and low R conditions, while equiaxed grains form under low G and high R conditions. On the other hand, in the austenitic 304 and 304L SSs (Figs. 5(a), 5(b), 6(a), and 6(b)) and the martensitic 403 and 410 SSs (Figs. 5(i), 5(j), 6(i), and 6(j)), equiaxed grains tend to form under high G and low R conditions, while columnar crystals tend to form under low G and high R conditions. This is the opposite trend to the CET criteria. Fluid flows tend to be faster under low R conditions, *i.e.*, solidification conditions for forming equiaxed grains are abundant. In the previous study,[33] we investigated the relationship between the solidification microstructure and solidification conditions in austenitic 304 and 316L SSs melted by electron beam irradiation, and a high fluid velocity during solidification is suggested to result in the formation of equiaxed grains by fragmentations of dendrites and the transport of the fragments.[36–38] This study indicates that a high fluid velocity promotes the formation of equiaxed crystals in SSs melted by laser beam irradiation, consistent with the findings for electron beam irradiation.

Figure 7 shows the average aspect ratio and average grain size (d) of the grains formed in the SSs plotted as a function of liquidus-solidus temperature difference (ΔT_0). The average aspect ratio and grain size were evaluated from the data obtained by EBSD analysis, and the liquidus/solidus ΔT_0 was calculated using JMatPro v11.2 software. The trends in the change in aspect ratio and grain size with respect to ΔT_0 differed significantly by SS type; in ferritic and martensitic SSs, the average aspect ratio decreased with increasing ΔT_0, consistent with the CET criteria. On the other hand,

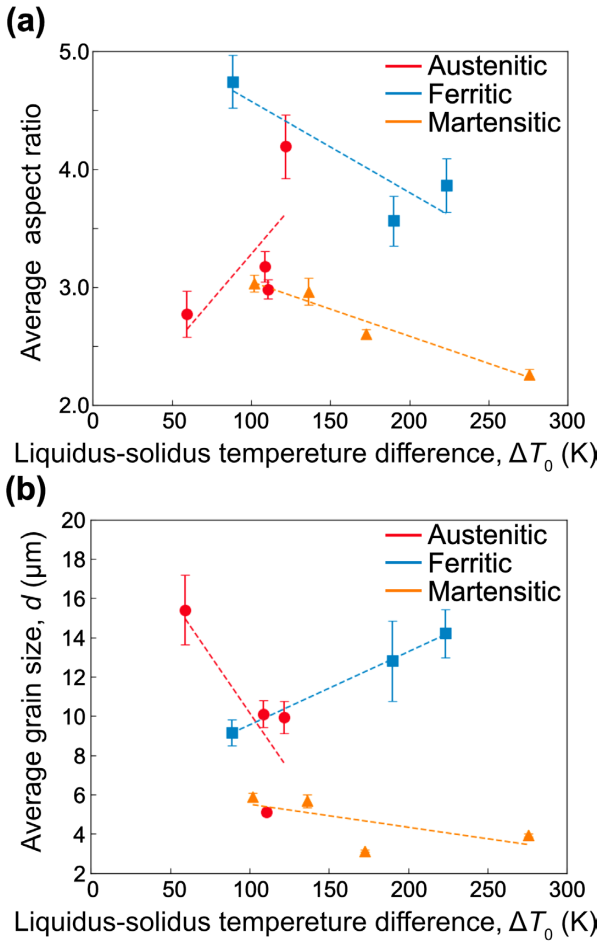

Fig. 7. (a) Average of aspect ratio and (b) average grain size plotted as a function of liquidus-solidus temperature differences ΔT_0. (Online version in color.)

in austenitic SSs, the average aspect ratio increased with increasing ΔT_0, which was the opposite trend to the CET criteria. In austenitic and martensitic SSs, the average grain size decreased with increasing ΔT_0. On the other hand, in ferritic SSs, the average grain size increased with increasing ΔT_0. **Table 4** summarizes the changes in the aspect ratios and grain sizes. It should be noted that the grain size and aspect ratio of the 403, 410, and 420J2 martensitic SSs were evaluated from the martensitic transformed microstructure observed via SEM-EBSD. The columnar or equiaxed tendency of the solidification microstructure is presumed to be qualitatively preserved in the aspect ratio, as martensite microstructures are morphologically constrained by the prior austenite grains. Conversely, grain size is likely influenced by refinement associated with the martensitic transformation. However, the relative comparison among the martensitic stainless steels remains valid because the solidification conditions are nearly identical across the alloys, as demonstrated by the CtFD simulations (Fig. 4), indicating that differences in grain size are due to alloy composition. These findings highlight the importance of tailored alloy design for each SS type based on application needs and provide a basis for guidelines on alloy selection and design to promote the formation of fine, equiaxed grains. Notably, 440C SS retained the FCC phase under rapid cooling in the PBF process due to its high carbon content, and detailed investigations into the mechanism of FCC phase formation in 440C are ongoing.

Table 4. Averages of aspect ratio and grain size for each steel obtained in this study.

	Grade	Aspect ratio Ave.	Aspect ratio Std.	Grain size Ave. (μm)	Grain size Std. (μm)
Austenitic	304	3.17	0.130	10.1	0.673
	304L	2.98	0.083	5.11	0.180
	316	4.19	0.270	9.94	0.826
	316L	2.77	0.192	15.4	1.763
	321	2.28	0.035	3.72	0.074
Ferritic	430	4.74	0.222	9.14	0.666
	443J1	3.86	0.228	14.2	1.228
	444	3.56	0.212	12.8	2.048
Martensitic	403	2.26	0.040	3.94	0.088
	410	3.03	0.073	5.89	0.167
	420J2	2.60	0.041	3.13	0.043
	440C	2.96	0.114	5.68	0.328

To obtain practical alloy design guidelines for controlling microstructures, the contribution of alloy elements to the aspect ratio and grain size was investigated by a data science approach, *i.e.*, random forest analysis. Data for 10 steels, excluding the 420J2 and 440C high-carbon steels, were used for the analysis. **Figures 8**(a) and 8(b) show the importance of each element to the aspect ratio and grain size. The coefficients of determination R^2 for the aspect ratio and grain size were 0.881 and 0.871, respectively. The Si concentration had the most significant contribution to the aspect ratio, with the C and Mn concentrations also contributing relatively significantly. On the other hand, the concentration of C had the most important effect on grain size, with the Mn concentration also contributing. Figures 8(c1)–8(d3) show the aspect ratio and grain size and the concentrations C, Mn, and Si, which exhibit a large contribution. The aspect ratio increased with increasing C concentration, while it decreased with increasing Mn and Si concentrations. These results suggest that a design guideline for an alloy with an equiaxed microstructure can be achieved by decreasing the C concentration and increasing the Mn and Si concentrations. However, no clear correlation can be seen between the concentration of these elements and the grain size. It is necessary to investigate the solidification microstructure formed by laser irradiation for SS samples with alloy compositions significantly different from the SSs investigated in this study to obtain guidelines for alloy design that control the grain size in the PBF process.

4. Conclusions

In this study, to clarify the relationship between alloy composition and microstructure formation in the laser PBF process, we investigated the microstructures of laser beam melt regions in 12 SSs: austenitic (304, 304L, 316, 316L, and 321), ferritic (430, 443J1, and 444), and martensitic (403, 410, 420J2, and 440C) SSs. The microstructures of the melt pools were analyzed using SEM-EBSD, and the

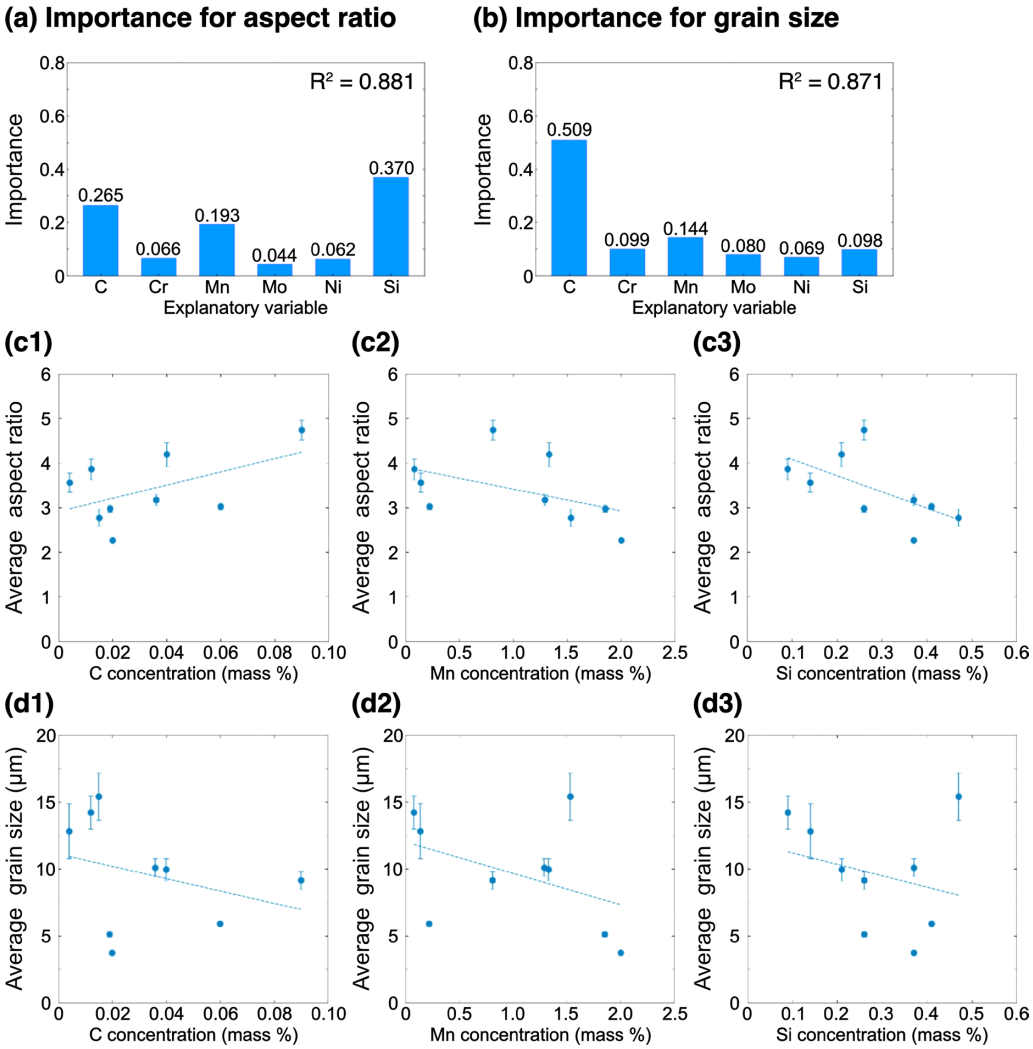

Fig. 8. Importances of each element for (a) average aspect ratio and (b) average grain size. (c1–c3) Average aspect ratio and (d1–d3) average grain size as a function of (c1,d1) C, (c2,d2) Mn, and (c3,d3) Si concentrations. (Online version in color.)

solidification conditions were evaluated using CtFD simulations. In ferritic and martensitic SSs, the grains became equiaxed as the liquidus-solidus temperature difference ΔT_0 increased, as in the CET criteria proposed by Hunt.[26] On the other hand, in austenitic SSs, the aspect ratio of the formed grains increased with increasing ΔT_0, which is the opposite trend to the CET criteria. Furthermore, the contribution of alloy compositions to the solidification microstructure was investigated using the machine-learning technique. The concentrations of Si, C, and Mn are revealed to significantly affect the aspect ratio, and an alloy design with reduced C concentration and increased Mn and Si concentrations is suggested to form a microstructure with a small aspect ratio.

Statement for Conflict of Interest

The authors declare that they have no known competing financial interests or personal relationships that could have appeared to influence the work reported in this paper.

Acknowledgments

This study was partly supported by ISIJ Research Promotion Grants from the Iron and Steel Institute of Japan (ISIJ), JSPS KAKENHI Grant Numbers 21H05018 and 21H05193, and CREST Nanomechanics: Elucidation of macroscale mechanical properties based on understanding nanoscale dynamics for innovative mechanical materials (Grant Number: JPMJCR2194) from the Japan Science and Technology Agency (JST). We would like to thank Mr. H. Kawabata and Mr. K. Kimura for their technical support in the sample preparation and laser beam irradiation experiments.

REFERENCES

1) M. Okugawa, S. Kanegae and Y. Koizumi: *Extrem. Mech. Lett.*, **77** (2025), 102319. https://doi.org/10.1016/j.eml.2025.102319
2) S. Kanegae, M. Okugawa and Y. Koizumi: *Materials*, **16** (2023), 6854. https://doi.org/10.3390/ma16216854
3) K. Cho, K. Yamashita, S. Kakutani, T. Saito, T. Sasaki, K. Sawaizumi, M. Okugawa, Y. Koizumi, T. Mayama, T. Kikukawa, O. Gokcekaya, T. Ishimoto, H. Kimizuka, W. Gong, T. Kawasaki, *et al.*: *Acta Mater.*, **303** (2026), 121696. https://doi.org/10.1016/j.actamat.2025.121696
4) H. Chen, D. Egusa, Z. Li, T. Sasaki, R. Ozasa, T. Ishimoto, M. Okugawa, Y. Koizumi, T. Nakano and E. Abe: *Addit. Manuf.*, **102** (2025), 104737. https://doi.org/10.1016/j.addma.2025.104737
5) S. Mino, M. Okugawa, T. Nakano and Y. Koizumi: *J. Japan Soc. Powder Powder Metall.*, **72** (2025), S1465. https://doi.org/10.2497/jjspm.16P-T6-11
6) S. Cai, R. Nagashima, Y.W. Chai, N. Sakaguchi and N. Nakada: *ISIJ Int.*, **65** (2025), 1201. https://doi.org/10.2355/isijinternational.ISIJINT-2025-058
7) N. Takata, Y. Ito, R. Nishida, A. Suzuki, M. Kobashi and M. Kato: *ISIJ Int.*, **64** (2024), 303. https://doi.org/10.2355/isijinternational.

ISIJINT-2023-045
8) P.V. Cobbinah, S. Matsunaga, Y. Toda, R. Ozasa, M. Okugawa, T. Ishimoto, Y. Liu, Y. Koizumi, P. Wang, T. Nakano and Y. Yamabe-Mitarai: *Smart Mater. Manuf.*, **2** (2024), 100050. https://doi.org/10.1016/j.smmf.2024.100050
9) M. Okugawa, Y. Isono, Y. Koizumi and T. Nakano: *Mater. Trans.*, **64** (2023), 37. https://doi.org/10.2320/matertrans.MT-MLA2022010
10) Y. Koizumi and M. Okugawa: *ISIJ Int.*, **62** (2022), 2183. https://doi.org/10.2355/isijinternational.ISIJINT-2022-184
11) M. Okugawa, Y. Furushiro and Y. Koizumi: *Materials*, **15** (2022), 6092. https://doi.org/10.3390/ma15176092
12) M. Okugawa, Y. Ohigashi, Y. Furishiro, Y. Koizumi and T. Nakano: *J. Alloys Compd.*, **919** (2022), 165812. https://doi.org/10.1016/j.jallcom.2022.165812
13) M. Okugawa, D. Izumikawa and Y. Koizumi: *Mater. Trans.*, **61** (2020), 2072. https://doi.org/10.2320/matertrans.MT-MA2020005
14) K. Sato, S. Takagi, S. Ichikawa, T. Ishimoto and T. Nakano: *Mater. Lett.*, **372** (2024), 136978. https://doi.org/10.1016/j.matlet.2024.136978
15) F. Sun, Y. Adachi, K. Sato, T. Ishimoto, T. Nakano and Y. Koizumi: *Materials*, **17** (2024), 1851. https://doi.org/10.3390/ma17081851
16) Y. Liu, K. Nose, M. Okugawa, Y. Koizumi and T. Nakano: *Mater. Trans.*, **64** (2023), 1135. https://doi.org/10.2320/matertrans.mt-me2022006
17) K. Sato, S. Takagi, S. Ichikawa, T. Ishimoto and T. Nakano: *Materials*, **16** (2022), 218. https://doi.org/10.3390/ma16010218
18) T. Ishimoto, S. Wu, Y. Ito, S.-H. Sun, H. Amano and T. Nakano: *ISIJ Int.*, **60** (2020), 1758. https://doi.org/10.2355/isijinternational.ISIJINT-2019-744
19) S.H. Sun, T. Ishimoto, K. Hagihara, Y. Tsutsumi, T. Hanawa and T. Nakano: *Scr. Mater.*, **159** (2019), 89. https://doi.org/10.1016/j.scriptamat.2018.09.017
20) Y.M. Wang, T. Voisin, J.T. McKeown, J. Ye, N.P. Calta, Z. Li, Z. Zeng, Y. Zhang, W. Chen, T.T. Roehling, R.T. Ott, M.K. Santala, P.J. Depond, M.J. Matthews, A.V. Hamza and T. Zhu: *Nat. Mater.*, **17** (2018), 63. https://doi.org/10.1038/nmat5021
21) T. Ishimoto, N. Morita, R. Ozasa, A. Matsugaki, O. Gokcekaya, S. Higashino, M. Tane, T. Mayama, K. Cho, H.Y. Yasuda, M. Okugawa, Y. Koizumi, M. Yoshiya, D. Egusa, T. Sasaki, E. Abe, *et al.*: *Acta Mater.*, **286** (2025), 120709. https://doi.org/10.1016/j.actamat.2025.120709
22) T. Takaki, Y. Takahashi and S. Sakane: *Mater. Trans.*, **64** (2023), 1150. https://doi.org/10.2320/matertrans.MT-ME2022014
23) K. Hagihara and T. Nakano: *JOM*, **74** (2021), 1760. https://doi.org/10.1007/s11837-021-04966-7
24) O. Gokcekaya, T. Ishimoto, S. Hibino, J. Yasutomi, T. Narushima and T. Nakano: *Acta Mater.*, **212** (2021), 116876. https://doi.org/10.1016/j.actamat.2021.116876
25) T. Ishimoto, K. Hagihara, K. Hisamoto, S.H. Sun and T. Nakano: *Scr. Mater.*, **132** (2017), 34. https://doi.org/10.1016/j.scriptamat.2016.12.038
26) J.D.D. Hunt: *Mater. Sci. Eng.*, **65** (1984), 75. https://doi.org/10.1016/0025-5416(84)90201-5
27) M. Gäumann, C. Bezençon, P. Canalis and W. Kurz: *Acta Mater.*, **49** (2001), 1051. https://doi.org/10.1016/S1359-6454(00)00367-0
28) W. Kurz, C. Bezençon and M. Gäumann: *Sci. Technol. Adv. Mater.*, **2** (2001), 185. https://doi.org/10.1016/S1468-6996(01)00047-X
29) M. Gäumann, R. Trivedi and W. Kurz: *Mater. Sci. Eng. A.*, **226–228** (1997), 763. https://doi.org/10.1016/S0921-5093(97)80081-0
30) M. Okugawa, Y. Furushiro, S. Motoyama, Y. Liu, T. Nakano and Y. Koizumi: *Mater. Trans.*, **67** (2026), 535. https://doi.org/10.2320/matertrans.MT-M2025132
31) M. Okugawa, H. Yoshima, Y. Liu, P. Wang, Y. Koizumi and T. Nakano: *Virtual Phys. Prototyp.*, **21** (2026), e2639906. https://doi.org/10.1080/17452759.2026.2639906
32) M. Okugawa, K. Saito, H. Yoshima, K. Sawaizumi, S. Nomoto, M. Watanabe, T. Nakano and Y. Koizumi: *Addit. Manuf.*, **84** (2024), 104079. https://doi.org/10.1016/j.addma.2024.104079
33) Y. Miyata, M. Okugawa, Y. Koizumi and T. Nakano: *Crystals*, **11** (2021), 856. https://doi.org/10.3390/cryst11080856
34) R. Rai, T. A. Palmer, J. W. Elmer and T. Debroy: *Welding Journal*, **88** (2009), 54.
35) Y. Zhang, J.R.G. Evans and S. Yang: *J. Chem. Eng. Data*, **56** (2011), 328. https://doi.org/10.1021/je1011086
36) Y. Zhao, Y. Koizumi, K. Aoyagi, D. Wei, K. Yamanaka and A. Chiba: *Addit. Manuf.*, **26** (2019), 202. https://doi.org/10.1016/j.addma.2018.12.002
37) T. Campanella, C. Charbon and M. Rappaz: *Metall. Mater. Trans. A*, **35A** (2004), 3201. https://doi.org/10.1007/s11661-004-0064-1
38) A. Hellawell, S. Liu and S.Z. Lu: *JOM*, **49** (1997), 18. https://doi.org/10.1007/BF02914650